Ultra-fast Thermoreflectance Imaging for Electronic, Optoelectronic, and Thermal Devices

Je-Hyeong Bahk¹ and Ali Shakouri²

¹Dept. of Mechanical and Materials Engineering, University of Cincinnati, Cincinnati, OH 45221, USA; bakkig@uc.edu
²Microsanj LLC, San Jose CA; and Birck Nanotechnology Center, Purdue University, West Lafayette IN 47907, USA, shakouri@purdue.edu

Abstract— We review the recent advances in thermal characterization of micro/nanoscale electronic, optoelectronic, devices based on thermoreflectance imaging. Thermoreflectance imaging is a non-invasive optical technique that can visualize surface thermal response of devices and integrated circuits (IC). Recent advances of the technique have enabled high-resolution, ultra-fast transient thermal imaging with 800 ps temporal resolution. Using visible or UV illumination, spatial resolution of about 200-250 nm can be achieved. Many IC substrates, e.g. Si, GaAs, are transparent to near IR illumination in 1-1.5 µm wavelength range. Through-substrate thermal imaging of flip-chip bonded ICs with micron spatial resolution has been demonstrated. We provide key examples of various devices characterized by the technique such as CMOS ICs, GaN HEMT, nanowire transistors, thin-film solar cells, and micro-thermal cloaking devices. In addition to the validation of electrothermal models, material and fabrication defects can be identified. Finally we discuss the advantages/limitations, and perspective of thermoreflectance imaging technique.

Keywords—Thermoreflectance imaging, thermal characterization, CMOS ICs, HEMT, thermal devices

I. INTRODUCTION

Performance and reliability of integrated circuits (ICs) and micro/nanoscale devices are highly related to device selfheating. [1] An understanding of thermal characteristics of these systems is therefore essential for device and chip-level optimization. Computational thermal simulations are helpful to guide design, but unexpected defects from materials or fabrication processes cannot be easily taken into account. Further miniaturization of devices into the nanoscale can promote nonconventional thermal responses in these devices, where ballistic thermal transport becomes significant, causing deviation from the Fourier law of thermal conduction. [2,3] The interface thermal resistances become highly relevant as well in nanoscale devices. [4] Moreover, the scaling down of device features results in a significant reduction in their thermal response time and an increase in their sensitivity to transient events. Hence, a nondestructive thermal imaging technique that offers ultra-high temporal and spatial resolutions can be a useful tool for optimizing the performance and reliability of modern and future devices of various kinds.

Charge-coupled device (CCD)-based thermo-reflectance imaging (TRI) is a convenient noninvasive optical technique that can perform surface temperature mapping on active micro/nanoscale devices. [5,6,7] Thermoreflectance is based

upon the detection of a variation in the optical reflectivity on the sample surface caused by a change in surface temperature. By converting the reflectivity change at each pixel, temperature mapping over the entire image can be obtained. Visible or UV illumination from light emitting diodes (LEDs) or laser diodes (LDs) is typically used as the light source, and the reflectivity change is sensed with a high-resolution CCD camera. Precise tuning of time delay between the electric device excitation and the LED pulse enables ultra-fast transient thermal imaging. The sensitivity and accuracy of this technique has been greatly improved over the past decade to achieve sub-nanosecond (800 ps) temporal resolution and submicron special resolution (200 ~ 250 nm) below the optical diffraction limit along with 50 mK temperature sensitivity. [8,9]

In this paper, we review the recent advances in the CCD-based thermoreflectance imaging technique and its application to various electronic, optoelectronic, and thermal devices. We focus on time-domain transient TRI only here. Frequency-domain CCD-based TRI is discussed elsewhere. [7,10] We first briefly overview the principles of TRI and the methods for ultra-fast transient thermal analysis with enhanced resolutions. Then, we discuss various recent TRI results for complementary metal-oxide-semiconductor (CMOS) integrated circuits (ICs), GaN high electron mobility transistors (HEMTs), semiconductor controlled rectifiers (SCRs), optically pumped gap plasmonic devices, waveguide Ge/Si photodetectors, thermoelectric microcoolers, and microscale thermal cloaking devices. Finally we provide the perspective of TRI technique before concluding the paper.

II. PRINCIPLES OF THERMOREFELCTANCE IMAGING

Fig. 1(a) shows a schematic system set-up for the CCD-based thermoreflectance imaging technique. A collimated narrow-band LED illuminates the surface of the device under test (DUT) through a microscope objective. Then the LED beam is reflected from the sample back to the objective and then to the CCD detector via a polarizing beam splitter (PBS). The collected image at the CCD detector is analyzed to obtain the optical reflectivity change from the 'cold' frame (with no DUT excitation) to the 'hot' frame (under DUT excitation). Since the reflectivity varies with the surface temperature, a temperature distribution $\Delta T(x,y)$ relative to the ambient induces a small change in the intensity of the reflected light that is captured by the CCD. The relative change in the reflectivity increases approximately linearly with the surface temperature, and thus can be quantified by a constant factor called the

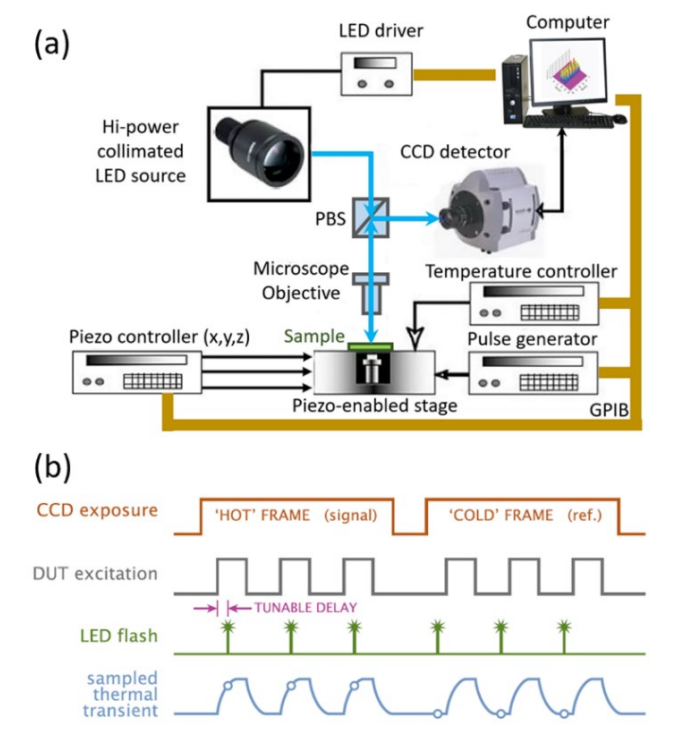


Fig. 1. (a) Schematic of a CCD-based thermoreflectance imaging system setup, and (b) schematic timing diagram for high-speed transient characterization.

thermoreflectance coefficient C_{TR} , such that $\Delta R/R = C_{TR}\Delta T$, where R is the reflectivity under no bias, ΔR is the change in the reflectivity under bias, and ΔT is the corresponding temperature rise. The measured reflectivity change is converted to ΔT at each location or each pixel with C_{TR} known a priori. The C_{TR} value is a material property that is a function of the illumination wavelength, typically on the order of 10^{-5} to 10^{-3} in the unit of K⁻¹, but also strongly influenced by the measurement apparatus, particularly by the magnification and numerical aperture of the optics. Thus, the C_{TR} must be carefully calibrated for at each location in each measurement. [11]

Fig. 1(b) displays a schematic timing diagram for the CCD exposure, device bias (DUT excitation), LED pulses, and the sampling of resulting thermal transients for time-domain thermoreflectance imaging. [12,13] synchronization between these signals is critical for imaging time-dependent temperature response of the device. This synchronization is performed by the system's timebase electronics. The CCD Camera synchronization is achieved using an electronic imaging shutter. The tunable time delay of the LED pulses relative to the device excitation determines the sampling time of temperature response, and is controlled for each camera exposure as shown in Fig. 1(b). A time series of thermal images can be captured by continuously shifting this time delay. A close-loop piezo-enabled sample stage is utilized to minimize the image blurring caused by the thermal expansion of device/stage, or the drift in microscopy at high magnifications. [14] The entire system is placed on an antivibration table for stable measurements.

III. IMPROVING RESOLUTION AND SENSITIVITY

There have been great efforts to improve the temporal and spatial resolutions as well as the temperature sensitivity and the signal-to-noise ratio for CCD-based thermoreflectance imaging systems. In this section, we discuss the physical background that determine these performance measures and the methods used to improve them.

A. Temporal resolution

Temporal or time resolution required in transient TRI is related to the length scale being investigated because heat diffusion is a function of time. If the temperature reading error is assumed to be 1 % or less, the required temporal resolution in the diffusive transport regime is equal to or less than $0.02l^2/\alpha$, where l is the length scale, and α is the thermal diffusivity of the material. [15] For instance, a length scale or spatial resolution of 2 μ m requires approximately 1 ns temporal resolution for pure silicon with 1 % temperature error. This implies that a sub-nanosecond temporal resolution is typically required for nanoscale devices made of silicon. Moreover, ballistic thermal transport can become significant in nanoscale devices, which may cause a faster thermal response than in the diffusive regime. [2]

The temporal resolution of a TRI system is determined by the smallest time step allowed for the tunable delay shown in Fig. 1(b), which in turn is determined by the pulse width of the light source. LED's are easily pulsed to 100 ns or shorter, and a pulsed laser can be used to image in the picosecond regime. Narrow-band LED sources of 365~530 nm peak wavelengths were used to achieve a 50 ns temporal resolution. [8,16] Recently, an ultra-short pulsed laser source of 440 nm wavelength was used for 800 ps resolution for transient thermal

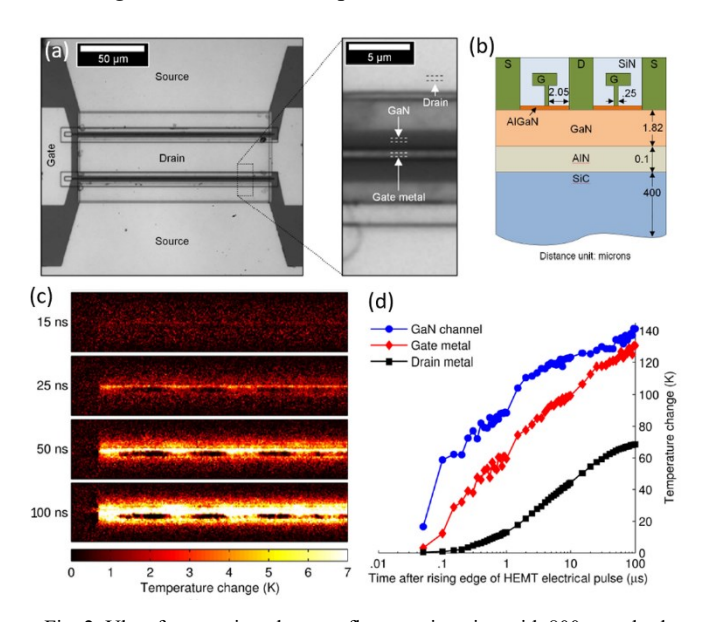


Fig. 2. Ultra-fast transient thermoreflectance imaging with 800 ps pulsed laser source for AlGaN/GaN HEMT RF power transistors. (a) Optical CCD image of the HEMT, (b) the schematic cross-section of the HEMT, (c) transient thermal images near the channel region within 100 ns time, and (d) the average temperature rise with time up to 100 µs after the rising edge of square bias at the three different regions. The deep channel temperature was obtained by micro-Raman thermography. Reprinted with permission from Ref. [9]. © 2014 IEEE.

analysis of AlGaN/GaN HEMT RF power transistors with 5 µm channel length. [9] The HEMT was electrically excited with periodic, low duty-cycle square voltage pulses, and the voltage pulses produced self-heating in the HEMT. As shown in the thermal image in Fig. 2(c), the self-heating starts to be visible on the gate metal within 15 ns after the bias is applied. The temperature rise was slower than anticipated by finite element simulations due to the internal interface thermal resistance. The TRI can capture this type of unknown effects in the model. [9]

B. Spatial resolution

At low magnifications, the spatial resolution of a TRI system is primarily determined by the pixel pitch of the CCD camera divided by the overall magnification of the optics. At high magnifications, the spatial resolution is limited by the optical diffraction. In the diffraction limit, the spatial resolution d is directly proportional to the wavelength λ and inversely proportional to the numerical aperture (NA), such that d = $\lambda/(2n\sin\theta)$, where n is the refractive index, and θ is the maximal half angle of the cone of light that can enter or exit the optics. The product $n \sin \theta$ is the numerical aperture. Standard air gap objectives have an upper NA limit of 1, leaving $d \sim \lambda/2$. Since the TRI system can use visible wavelengths that are much shorter than those of infrared, its spatial resolution is typically better than infrared thermography techniques. For the typical visible wavelengths of LEDs used in TRI, the spatial resolution is on the order of $300 \sim 400$ nm. When a UV light of 365 nm is used, the spatial resolution becomes lower to be ~ 260 nm for NA = 0.7. Most of the TRI systems use standard visible light illuminations due to the simplicity in optics. Pushing further into UV illumination may require special optics such as fused silica or UV anti-reflective coating objectives to improve light transmission and reduce optical aberrations. [17]

Another reason to use UV illumination other than for better spatial resolution is that the penetration depth of shorter wavelength is shallower, which can avoid unwanted influence from deeper layers in the reflectivity measurement. For instance, the 530 nm visible light produced a strong signal at the top of the gate metal as shown in Fig. 3 (top row), but the signal was much weaker at the trench region where the thin GaN channel on SiC substrate is exposed, due to the significant light absorption through the deep layers in this region. [17] On

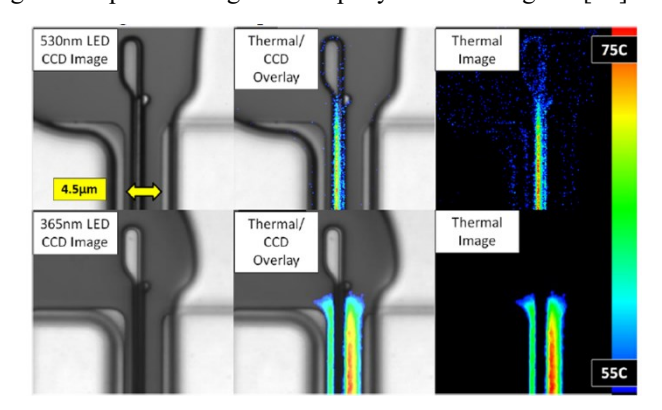


Fig. 3. Thermoreflectance imaging of GaN//SiC HEMTs near the gate region with both 530 nm visible green (top row) and 360 nm UV (bottom row) illumination: their optical images (left), thermal images (right), and their overlaid pictures (middle). Reprinted with permission from Ref. [17]. © 2018 IEEE.

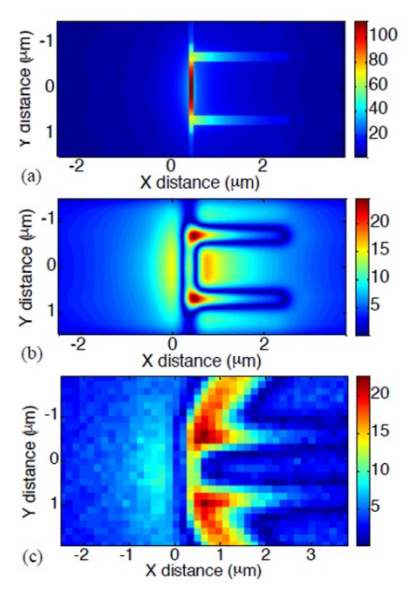


Fig. 4. (a) Real temperature profile from ANSYS finite element simulation for a 100 nm wide metal heater line. (b) Blurred image of the first image by the Gaussian blurring algorithm, and (c) the actual TRI image from a 100 nm metal heater line that is diffraction limited under 100x magnification and NA = 0.7 with 530 nm wavelength. Image (b) and (c) resemble each other. Reprinted with permission from Ref. [18]. © 2015 IEEE.

the other hand, a 365 nm UV illumination (bottom row) significantly reduced the convolution from the deeper layers, and achieved a strong signal sensitivity with a high C_{TR} in the trench region, along with a better spatial resolution. By combined TRI with the two wavelengths, a complete temperature profile across the channel and gate region is obtained.

Recently, there have been efforts to reconstruct real thermal images from diffraction-limited blurred TRI images using postimage processing methods. Ziabari et al. [18] used a Gaussian blurring algorithm to successfully convert an ANSYS simulated thermal image (Fig.4(a)) to a blurred image (Fig.4(b)) that resembles the diffraction-limited TRI image (Fig.4(c)) for a 100 nm wide metal heater line. They suggested as a future work to develop a de-blurring post-processing algorithm to reconstruct the real thermal image from the diffraction-limited image obtained by TRI. More work is needed for developing the de-blurring algorithm.

Other than the fundamental diffraction limit, image shifts and instrument drifts can also limit the spatial resolution. These unwanted movements can cause sample regions made of different materials or with different C_{TR} values to overlap with each other in the final TRI image, which makes the TRI analysis difficult. As the feature sizes shrink further, this issue becomes more important, ultimately limiting the spatial resolution. To overcome this issue, Shakouri et al. [14] proposed to use a piezoelectric sample stage that can automatically adjust the sample position relative to the illumination, based on the feedback from the concurrent optical image obtained during the TRI measurement. This piezo-stage can adjust the position in all the three axes to correct defocusing in the vertical axis and lateral shifts as well. A nanoscale heater line of 100 nm width

that is well under the diffraction limit was tested with the piezostage and reproducible TRI images were obtained. [14]

C. Temperature resolution and signal-to-noise ratio

In a TRI system, photon short noise in the CCD camera is the dominant noise mechanism because of the weak illumination from the short LED pulses. We are looking at a very small change in reflectivity, ΔR , riding on a relatively large absolute reflectivity R. In the small ΔR signal, short noise can be comparably large. This shot noise gives rise to random intensity fluctuations, which can be reduced through heavy averaging over an extended period of time with repeated pulse trains. According to Shakouri et al. [19] the signal to noise ratio (SNR) of the measurement increases with the square root of the number of averages taken N as in SNR $\propto \sqrt{N}$. The noise level measured by the standard deviation of ΔT was lowered below 20 mK after about 20 minutes of averaging on a 3500 pixel area under 50x magnification on a gold metal line with small or no heating.

To obtain a reasonable SNR in the TRI image, the total reflected light that is recorded in the CCD must exceed a minimum intensity. This minimum required intensity is typically much greater than the reflected light intensity from a single LED pulse. Therefore, many LED pulses must be illuminated and added per each CCD frame, so that the total accumulated intensity can be much greater than the minimum per frame. Typically the LED is run at a 1% duty cycle, and the device at 25%. Device excitation is usually kept much below 50% duty cycle to ensure the device to be cooled back to room temperature before the next heating cycle. [10]

IV. THERMAL IMAGING RESULTS OF VARIOUS DEVICES

A. Front-side and through-substrate thermal imaging of logic ICs

TRI is very useful for nondestructively detecting faults in ICs during operation. Fig. 5 shows an example of a logic IC

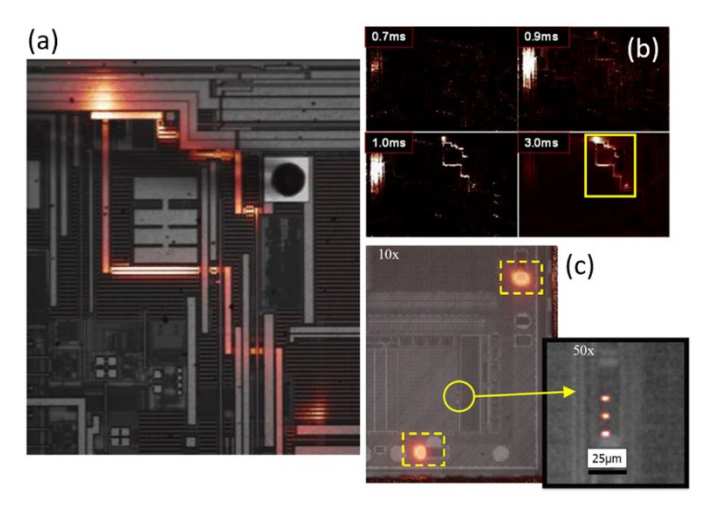


Fig. 5. Thermal images of a logic IC chip under bias. (a) superimposed thermal and optical images showing the heating regions on the front side of the chip, (b) transient thermal images on the front side from 0.7 to 3.0 ms, and (c) through-substrate thermal images obtained using near-infrared (NIR) illumination (1300 nm) superimposed on the optical image of the back side of the chip. Reprinted with permission from Ref. [6] Copyright 2013 ASM International.

measured by TRI. [6] As shown in Fig. 5(b), a heating begins as early as 0.7 ms after the chip starts on the left side of the chip, which is a normal operation. However, after 0.9 ms, another heating along narrow paths starts to occur on the right hand side of the chip and becomes dominant hot spots by 3 ms from the chip start. This right-side heating turned out to be an unexpected latch-up failure located at the bottom right part of the image.

Fig. 5(c) shows another thermal images of an IC obtained by TRI. This time, thermal images were obtained through the substrate at the backside of the chip. This was possible by using near-infrared (NIR) LED illumination of 1300 nm wavelength in TRI, which can penetrate through the silicon substrate due to its low absorption. Three small hot spots were observed in the middle of the image, which corresponds to three uncooled InGaAs array sensors that were actively emitting photons. Larger isolated hot spots were found at two locations marked by yellow rectangles in Fig. 5(c), which were induced by high current concentration of power lines during normal chip operation. [6]

B. Snapback in Semiconductor controlled rectifiers

On-chip electrostatic discharge (ESD) protection can be achieved using semiconductor controlled rectifiers (SCRs). When the SCR is supplied with an extremely high voltage pulse above the breakdown voltage by ESD, drain-gate capacitive coupling triggers the SCR into snapback mode. In this mode, the SCR undergoes unstable period ($10\sim100~\rm ns$) of changing device internal resistance, then stabilizes at a hold voltage much below the breakdown voltage and a current after about $100~\rm ns$.

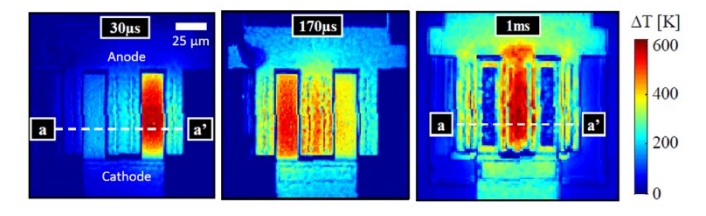


Fig. 6. Transient TRI images of a ESD protection SCR device in its snapback mode at current I = 1.22 A at 30 μ s, 170 μ s, and 1 ms (from left to right) after the rising edge of the device excitation. Reprinted with permission from Ref. [20]. © 2011 IEEE.

Transient TRI was conducted for a SCR after the snapback mode is reached after 100 ns, and the thermal images are shown in Fig. 6 at 30 μs , 170 μs , and 1 ms after the rising edge of the excitation pulse. [20] A clear time dependent heating is shown in the figure. In the time regime from 30 to 170 μs , the self-heating increases to $\Delta T \sim 400$ K, and the dominant heating spot switches from the right cathode finger to the left finger. This indicates high-speed current localization or non-simultaneous triggering of different finger junctions in the snapback mode of SCR. After steady-state is reached at 1 ms, heating is observed to spread to the anode fingers and become symmetric in the device.

C. Self-heating in Gate-all-around nanowire transistors

Nanowire MOSFETs with gate-all-around (GAA) geometry are a promising candidate for sub-10 nm technology nodes. [21] However, the GAA geometry is susceptible to the increased self-heating due to the poor heat dissipation from the nanowire

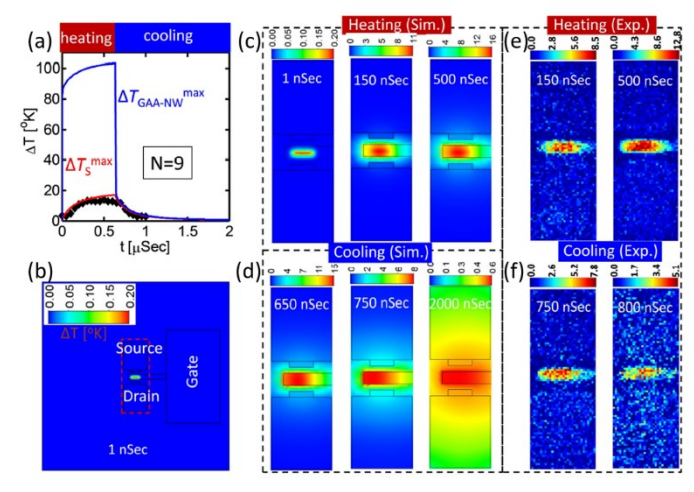


Fig. 7. Finite element simulation results ((c) and (d)) and TRI images ((e) and (f)) with λ =530 nm, 50 ns resolution for 30 nm InGaAs nanowire MOSFETs. The gate metal pad dimensions are 1 μ m × 7 μ m (W × L). (a) Temperature rise as a function of time inside the nanowire and the surface. Reprinted with permission from Ref. [22]. © 2015 IEEE.

to the substrate. Wahab et al. [22] combined 3D finite-element simulation with transient TRI to study the self-heating in GAAtype InGaAs nanowire MOSFETs. The cross-section of InGaAs nanowire channel was 30 nm × 30 nm square, and the length was 200 nm. The nanowires were surrounded by atomiclayer-deposited (ALD) alumina (Al₂O₃) gate insulator of 10 nm thickness, and the gate metal was tungsten nitride (WN). Since the nanowires are embedded in the structure underneath the gate metal, it was not possible to directly measure the temperature of the nanowire from the surface using TRI. Therefore, a full 3D finite element simulation was conducted to estimate the internal temperature rise in the nanowires based on the experimental surface temperature obtained from TRI. TRI was able to accurately measure temperature on the 1 µm wide gate metal pad with 50 ns temporal resolution. Some unknown properties such as interface thermal resistances were determined by fitting the surface temperature with the TRI results to accurately determine the internal heating. As shown in Fig. 7, the surface temperature rises to steady-state $\Delta T \sim 20$ K within ~500 ns. [22] The internal nanowire temperature was estimated to rise by 100 K. This shows a good example of TRI application reinforced by simulation studies.

D. Optically pumped gap plasmonic streutures

TRI can be useful for plasmonic devices. Wang et al. [23] developed a new TRI system with optical excitation instead of

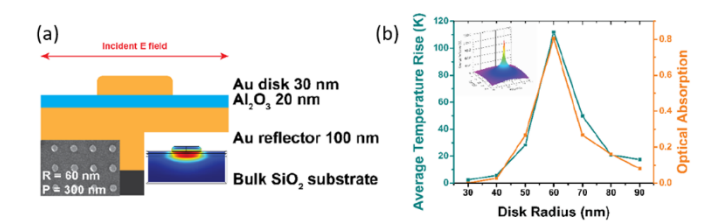


Fig. 8. TRI results of optically pumped gap plasmonic structures. (a) schematic cross-section of the disk-type device and a SEM picture of the disk array (bottom left), and the heat distribution cross-section by FEM simulation (bottom right). (b) Average steady-state temperature rise measured by TRI and optical absorption as a function of disk radius. Figures from Ref. [23].

electric device excitation to study self-heating in optically pumped gap plasmonic devices. Fig. 8(a) shows the cross-sectional schematic of the disk-type plasmonic structures and a SEM picture of the disk arrays with varying radius from 30 nm to 90 nm. The nanoscale gap between the top gold disk and the bottom gold reflector layer promotes plasmonic absorption, which then is dissipated as heat. This heating could be observed by the CCD-based TRI setup. The disks were excited by a continuous-wave (CW) 825 nm laser. As shown in Fig. 8(b), the 60 nm radius showed the largest temperature rise according to the TRI measurement, which corresponds to the maximum optical absorption at the radius.

E. Waveguide Ge/Si Photodiode

Performance of optoelectronic devices are sensitive to the internal temperature. Models are normally established based on the assumption of uniform temperature distribution, but determining the heat distribution in optoelectronic devices particularly for waveguide detectors is very difficult because the absorption profile is highly non-uniform, which can lead to localized heating at the input. Piels et al. [24] studied the non-uniform heating effects in Ge/Si waveguide photodiode using TRI and finite element simulation. A 627 nm red LED was used for the TRI. Optical illumination of 80 mW was left constant, and the bias voltage was modulated from 0 to −5 V at 400 Hz with 10% duty cycle.

As shown in Fig. 9, temperature distribution is highly non-uniform in the waveguide detector with localized heating at the input side (bottom side of the figure). The peak temperature reached $\sim 200\,^{\circ}\text{C}$ at the entrance. The change in temperature along the waveguide (vertical direction) roughly agrees with the absorption profile. The experimental surface temperature from TRI decreased more rapidly than the simulated surface temperature along the waveguide, which implies that the absorption coefficient of Ge used in the simulation (4000 cm $^{-1}$) was lower than the actual value. Fitting of the TRI data with

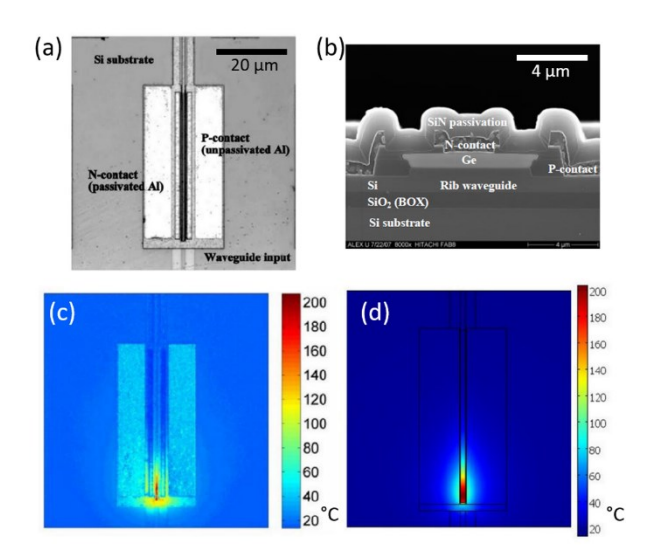


Fig. 9. TRI results of a Ge/Si waveguide photodiode. (a) optical image of the device (top view), (b) cross-sectional SEM picture of the device, and temperature distributions (c) from TRI, and (d) from finite element simulation. Figures from Ref. [24].

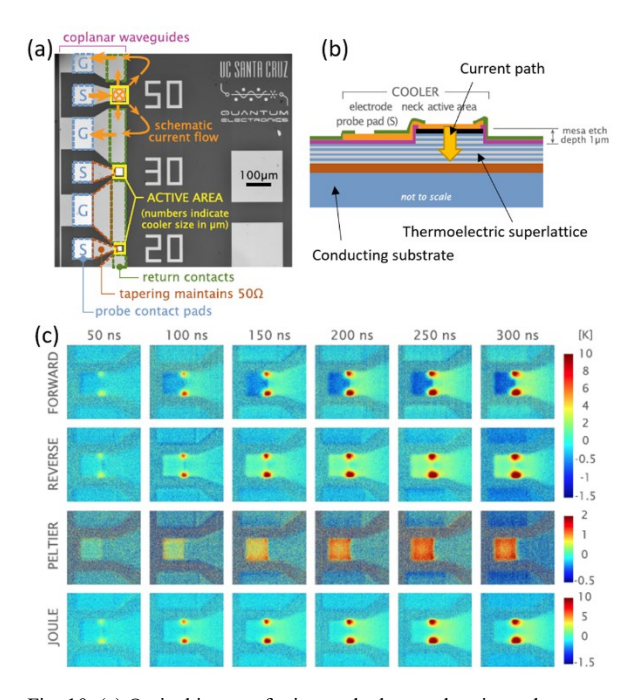


Fig. 10. (a) Optical image of microscale thermoelectric cooler array and (b) schematic cross-section of one cooler device. (c) Thermal images with 50 ns time intervals with forward (first row) and reverse (second row) bias from transient TRI. Magnitudes of separated Peltier and Joule components are also displayed in the third and fourth rows, respectively. Reprinted with permission from Ref. [13].

Copyright 2013 AIP Publishing.

simulation could be used to obtain the correct absorption coefficient of 4570 cm⁻¹.

F. High speed thermoelectric micro-cooler

Microscale thermoelectric coolers are useful for targeted hot-spot cooling in electronics. With electric current input, a micro-cooler device can cool down one side and heat up the other side by the Peltier effect. Vermeersch et al. [13] fabricated thermoelectric micro-coolers made of vertically stacked multilayer superlattices. In this device, current can be injected from the top metal contact and flow vertically through the superlattice device and the conducting substrate to the other side contact pad. The device picture and the cross-sectional schematic are shown in Fig. 10(a) and (b). The top surface of the device is cooled down due to the Peltier cooling, which could be observed by TRI.

Fig. 10(c) shows the transient TRI images obtained with 50 ns intervals. With forward bias, the top surface was cooled down and with reverse bias, the top surface was heated up. There were two prominent hot spots at the neck of the top metal contact that climbs the sidewall of the device mesa from the lower surface. At the neck, the metal layer was much thinner than the normal thickness, which caused larger resistance around it and thus a larger Joule heating. These hot spots were not visible in the Peltier component of the temperature profile (the third row of Fig. 10(c)) bud shown only in the Joule component according to the TRI measurements, confirming the increased Joule heating at the neck. In this work, the Peltier and Joule components could be separated from the overall thermal image by two measurements with opposite current directions.

By flipping current direction, the Peltier component flips its direction, while the Joule component doesn't. By taking the difference between the two thermal images with opposite current directions, the Peltier component can be extracted, and the rest of it is the Joule component.

G. Microscale thermal cloaking device

Microscale thermal devices that can manipulate thermal transport as modern electronics do to electron transport have drawn great attention in recent years. [25] One recent example is the micro-thermal cloaking devices fabricated on thin suspended membranes by focused ion beams. [26] High energy focused He ion beams created micro/nano patterns on Si membrane to alter the thermal conductivity of the exposed region over a wide range. This way, Choe et al. [26] created thermal cloaking devices with circular patterns of suppressed thermal conductivities as shown in Fig. 11. Due to the low thermal conductivity region surrounding the core area, heat flow goes around the circular region without affecting the core area, so thermally cloaking. The modified temperature and heat flux distributions were obtained by steady-state TRI, which confirmed the predicted results from finite element simulation. This work showcases the usefulness of TRI technique for the study of microscale thermal devices, where noncontact, ultrahigh resolution thermal analysis is required.

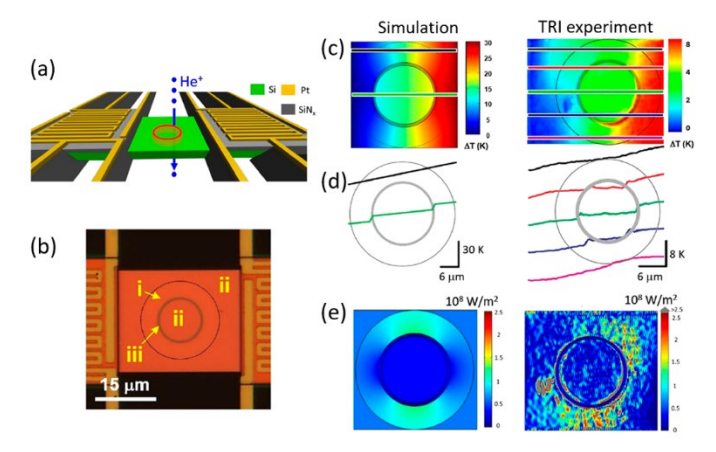


Fig. 11. (a) Schematic of micro thermal cloaking device fabricated on thin Si membrane with He ion beams. Two heaters are fabricated at both sides to create heat flow for the experiment. (b) a SEM image of the actual device showing the circular patterns created by the focused ion beams. (c) Simulated and measured temperature distribution, (d) temperature curves along the horizontal lines shown in (c), and (e) simulated and measured heat flux distribution. Reprinted with permission from Ref. [26]. Copyright 2019

American Chemical Society.

V. SUMMARY AND OUTLOOK

In this paper, we have reviewed the state-of-the-art CCD-based thermoreflectance imaging technique and its application to various electronic, optoelectronic, and thermal devices. Since TRI is non-contact and non-invasive, it enables ultra-fast thermal analysis of a wide range of micro/nano devices and chip-level fault inspection. Ultra-fast transient thermal imaging has been achieved for 50 ns temporal resolution using narrowband LED sources, and 800 ps resolution using a pulsed laser source. The spatial resolution has been substantially improved down to 200 nm by shorter wavelength UV illumination. Stable measurements are achieved by minimizing instrument drift and

sample movements during the measurement using real-time piezoelectric control of the sample stage, which helps improve the spatial resolution. As a future work, advanced image denoising and deblurring techniques can be combined with piezo-controlled mechanical stage to improve the image quality.

Attempts to beat the diffraction limit have been made to further improve the spatial resolution. This is based on image de-convolution algorithms applied to the blurred thermal images due to the optical diffraction in order to reconstruct the real thermal images at the nanoscale. Further work to improve the convergence of the algorithm for diverse thermal maps may be able to push the spatial resolution to sub 100 nm. Improving the signal-to-noise ratio is also an important future work. Two tracks should be investigated; first, improving the hardware particularly the CCD camera and the illumination to minimize the shot noise, and second, further advancing the image denoising techniques. Either way, the improved performance of TRI will have a big impact in thermal characterization and other lock-in imaging applications.

ACKNOWLEDGMENT

This work is partially supported by NSF under Grant DMR-1905571.

REFERENCES

- S. V. Garimella et al., "Thermal Challenges in Next-Generation Electronic Systems," *IEEE Trans. Compon. Packag. Technol.*, vol. 31, no. 4, pp. 801-815, Dec. 2008.
- [2] A. Ziabari et al., "Full-field thermal imaging of quasiballistic crosstalk reduction in nanoscale devices," *Nat. Comm.*, vol. 9, p. 255, 2018.
- [3] B Vermeersch, AMS Mohammed, G Pernot, YR Koh, and A Shakouri, "Superdiffusive heat conduction in semiconductor alloys. II. Truncated Lévy formalism for experimental analysis," *Phys. Rev. B*, vol. 91, p. 085203, 2015.
- [4] Y. R. Koh et al., "Quasi-ballistic thermal transport in Al0.1Ga0.9N thin film semiconductors," Appl. Phys. Lett., vol. 109, p. 243107, 2016.
- [5] P. M. Mayer, D. Lüerssen, R. J. Ram, and J. Hudgings, "Theoretical and experimental investigation of the thermal resolution and dynamic range of CCD-based thermoreflectance imaging," *J. Opt. Soc. Am. A. Opt. Image Sci. Vis.*, vol. 24, p. 1156, 2007.
- [6] K. Yazawa, D. Kendig, and A. Shakouri, "Time-Resolved Thermoreflectance Imaging for Thermal Testing and Analysis," in Proc. the 39th International Symposium for Testing and Failure Analysis (ISTFA), San Jose, CA, USA, 2013, pp. 194-202.
- [7] M. Farzaneh et al., "CCD-based thermoreflectance microscopy: principles and applications," *J. Phys. D: Appl. Phys.*, vol. 42, no. 14, p. 143001, 2009.
- [8] D. Kendig et al., "Accurate Thermoreflectance Imaging of Nano-Features Using Thermal Decay," in Proc. IEEE 16th Intersociety Conference on Thermal and Thermomechanical Phenomena in Electronic Systems (ITherm), Orlando, FL, USA, 2017, p. 23.
- [9] K. Maize et al., "High Resolution Thermal Characterization and Simulation of Power AlGaN/GaN HEMTs Using Micro-Raman Thermography and 800 Picosecond Transient Thermoreflectance Imaging," in Proc. IEEE Compound Semiconductor Integrated Circuit Symposium (CSICS), La Jolla, CA, USA, 2014.
- [10] B. Vermeersch, J. Christofferson, K. Maize, A. Shakouri, and G.D. Mey, "Time and Frequency Domain CCD-Based Thermoreflectance Techniques for High-Resolution Transient Thermal Imaging," in *Proc. the 26th IEEE SEMI-THERM Symposium*, San Jose, CA, USA, 2010, p. 228.

- [11] T. Favaloro, J.-H. Bahk, and A. Shakouri, "Characterization of the temperature dependence of the thermoreflectance coefficient for conductive thin films," *Rev. Sci. Instrum.*, vol. 86, p. 024903, 2015.
- [12] J. Christofferson, Y. Ezzahri, K. Maize, and A. Shakouri, "Transient Thermal Imaging of Pulsed-Operation Superlattice Micro-Refrigerators," in *Proc. the 25th IEEE SEMI-THERM Symposium*, San Jose, CA, USA, 2009, p. 45.
- [13] B. Vermeersch, J.-H. Bahk, J. Christofferson, and A. Shakouri, "Thermoreflectance imaging of sub 100 ns pulsed cooling in high-speed thermoelectric microcoolers," *J. Appl. Phys.*, vol. 113, p. 104502, 2013.
- [14] A. Shakouri et al., "Stable Thermoreflectance Thermal Imaging Microscopy with Piezoelectric Position Control," in *Proc. the 32nd SEMI-THERM Symposium*, San Jose, CA, USA, 2016, p. 128.
- [15] K. Yazawa et al., "High Speed Transient Thermoreflectance Imaging of Microelectronic Devices and Circuits," EDFA Magazine, vol. 15, pp. 12-22, 2013.
- [16] C. Matei, P. Aaen, and D. Kending, "High-Resolution Thermoreflectance Imaging of GaN Power Microwave Transistors," in Proc. ARMMS RF & Microwave Society Conf., Wyboston Lakes, Wyboston, 2017.
- [17] D. Kendig et al., "UV Thermal Imaging of RF GaN Devices with GaN Resistor Validation," in Proc. the 91st ARFTG Microwave Measurement Conference (ARFTG), Philadelphia, PA, USA, 2018.
- [18] A. Ziabari et al., "Sub-diffraction Limit Thermal Imaging for HEMT Devices," in *Proc. the 31st SEMI-THERM Symposium*, San Jose, CA, USA, 2015, p. 82.
- [19] A. Shakouri et al., "Temperature Sensitivity and Noise in Thermoreflectance Thermal Imaging," in *Proc. the 31st SEMI-THERM Symposium*, San Jose, CA, USA, 2015, p. 216.
- [20] K. Maize, K. Kendig, A. Shakouri, and V. Vashchenko, "Nanosecond transient thermoreflectance imaging of snapback in semiconductor controlled rectifiers," in *Proc. International Reliability Physics* Symposium, Monterey, CA, USA, 2011, p. EL.4.
- [21] S. H. Shin et al., "Impact of nanowire variability on performance and reliability of gate-all-around III-V MOSFETs," in *Proc. IEEE International Electron Devices Meeting (IEDM)*, Washington, DC, USA, 2013, p. 7.5.1.
- [22] M. A. Wahab, S. H. Shin, and M. A. Alam, "3D Modeling of Spatiotemporal Heat-ransport in III-V Gate-all-around Transistors Allows Accurate Estimation and Optimization of Nanowire Temperature," *IEEE Trans. Electron Dev.*, vol. 62, p. 3595, 2015.
- [23] D. Wang et al., "Thermoreflectance Imaging of Optically Pumped Gap Plasmon Structures," in *Proc. Conference on Lasers and Electro-Optics (CLEO)*, San Jose, CA, USA, 2018, p. FTh1K.8.
- [24] M. Piels et al., "Three-dimensional Thermal Analysis of a Waveguide Ge/Si Photodiode," in *Proc. Integrated Photonics Research, Silicon and Nanophotonics*, Monterey, CA, USA, 2010, p. ITuA5.
- [25] G. Wehmeyer, T. Yabuki, C. Monachon, J. Wu, and C. Dames, "Thermal diodes, regulators, and switches: Physical mechanisms and potential applications," *Appl. Phys. Rev.*, vol. 4, p. 041304, 2017.
- [26] H.S. Choe et al., "Ion Write Microthermotics: Programing Thermal Metamaterials at the Microscale," *Nano Lett.*, vol. 19, no. 6, pp. 3830-3837, 2019.